

PAPER • OPEN ACCESS

Calibration of 3D scan trajectories for an industrial computed tomography setup with 6-DOF object manipulator system using a single sphere

To cite this article: Lorenz Butzhammer *et al* 2023 *Meas. Sci. Technol.* **34** 015403

View the [article online](#) for updates and enhancements.

You may also like

- [Extrinsic calibration method for 3D scanning system with four coplanar laser profilers](#)
Hangbo Zou, Renbo Xia, Jibin Zhao et al.
- [A multibody approach for 6-DOF flight dynamics and stability analysis of the hawkmoth *Manduca sexta*](#)
Joong-Kwan Kim and Jae-Hung Han
- [Modeling and control of magnetorheological 6-DOF stewart platform based on multibody systems transfer matrix method](#)
Min Jiang, Xiaoting Rui, Wei Zhu et al.

Calibration of 3D scan trajectories for an industrial computed tomography setup with 6-DOF object manipulator system using a single sphere

Lorenz Butzhammer* , Andreas Michael Müller  and Tino Hausotte 

Chair of Manufacturing Metrology, Friedrich-Alexander-Universität Erlangen-Nürnberg,
Nägelsbachstraße 25, 91052 Erlangen, Germany

E-mail: Lorenz.Butzhammer@fmt.fau.de

Received 3 August 2022, revised 26 September 2022

Accepted for publication 7 October 2022

Published 28 October 2022



CrossMark

Abstract

In industrial x-ray computed tomography (CT), the application of more complex scan paths in comparison to the typical circular trajectory (360° rotation of the measurement object) can extend the potential of CT. One way to enable such 3D scan trajectories is to use a 6-degrees-of-freedom (DOF) object manipulator system. In our case, a hexapod is mounted on top of the rotary table of a commercial CT scanner. This allows for adaptive tilting of the measurement object during the scan. For high accuracy, the geometry calibration of such setups is typically done using the x-ray projections of a calibrated multi-sphere object. Contrary to this, here, we demonstrate a procedure that is based on only a single sphere and can therefore experimentally be implemented with low effort. Using the intrinsic geometry parameters of the CT device as prior information, the hexapod coordinate system with respect to the CT machine coordinate system is determined by means of a one-step optimization approach. The resulting parameters are used to calculate projection matrices that enable the volume reconstruction for 3D scan trajectories. The method is validated using simulated x-ray images and experimental investigations including dimensional measurements. For the used setup, geometric measurement results for 3D scan trajectories that are calibrated with the presented method show in sum increased errors compared to the circular scans. A limited pose accuracy of the manipulator system is discussed as a potential cause. The results nevertheless indicate that the presented method is generally feasible for dimensional CT measurements provided that the pose accuracy is sufficient. The calibration procedure can therefore be a low-cost and easier to implement alternative compared to trajectory calibration methods based on multi-sphere objects, but with a tendency towards lower measurement accuracy. The methodology can in principle be transferred to different setups with 6-DOF manipulator systems, e.g. C-arm CT devices with a robot arm.

* Author to whom any correspondence should be addressed.



Original Content from this work may be used under the terms of the [Creative Commons Attribution 4.0 licence](https://creativecommons.org/licenses/by/4.0/). Any further distribution of this work must maintain attribution to the author(s) and the title of the work, journal citation and DOI.

Supplementary material for this article is available [online](#)

Keywords: x-ray computed tomography, dimensional metrology, scan trajectory, 6-DOF manipulator, hexapod, geometry calibration

(Some figures may appear in colour only in the online journal)

1. Introduction

X-ray computed tomography (CT) is an established technology in the field of nondestructive testing and dimensional metrology. Cone-beam CT devices equipped with an x-ray tube, a flat panel detector and a manipulator system including a rotary table form the most widespread device class in an industrial context [1]. Typically, a full 360° rotation of the measurement object is performed by the rotary table during the scan. Regarding the volume reconstruction as the most important post-processing step, the object rotation can be handled the same way as a rotation of the x-ray source and detector around the object in the opposite direction. Therefore, the motion is oftentimes described as a circular scan trajectory of the source, in analogy to medical CT devices. Strictly speaking, the position and orientation of the detector are additionally required to fully describe the geometry of the scan trajectory.

In recent years, there is a trend towards extending scan trajectories to task-specific, non-planar shapes, especially for large measurement objects that are scanned with the help of robot arms as manipulator systems for the x-ray tube and detector [1–4]. Particularly with focus on such setups, there are several publications dealing with different methods to optimize 3D scan trajectories for industrial CT with regard to imaging quality and measurement time [5–7].

3D scan trajectories could also be helpful for the measurement of smaller objects if cone-beam artifacts or spatially distributed, high absorbing components lead to image degradation and high measurement errors in case of the circular scan trajectory.

In a recent article [8], we showed that extending a commercial cone-beam CT scanner with a hexapod as 6-degrees-of-freedom (DOF) object manipulator is one possible technical implementation. To reach high metrological accuracy, the trajectory of the combined setup must be accurately determined. In [8], the pose of the measurement object (or rather of a coordinate system that is moved with the measurement object) was directly extracted projection-wise by repeating the scan with a multi-sphere object with calibrated sphere center positions. The projected sphere positions detected in the radiographs were used for an optimization approach to extract the geometry parameters, similar as in a standard CT geometry calibration procedure [9], but keeping the intrinsic parameters of the CT device (such as the source-detector-distance) fixed and only optimizing the pose of the reference object. This way, the additional axes of the hexapod did not deteriorate the dimensional measurement accuracy significantly.

The methodology was based on a theoretical background that is also used for camera pose estimation in the field of optical imaging, see e.g. [10]. In the field of CT, geometry

calibration with a multi-sphere object based on this background is well established and oftentimes used in the internal calibration routines provided by the CT manufacturers. A detailed implementation guide for a standard procedure using only a single projection can be found in [9]. Bircher *et al* [11] applied multi-sphere-based geometry calibration using different magnifications to increase the accuracy for metrological CT. Similar methods were used by Ferrucci *et al* [12], who focused on determining sample stage error motions.

Multi-sphere calibration of 3D scan trajectories, as performed in [8], shows high accuracy but also has some drawbacks.

First, the sphere center positions must be known, which typically requires calibration with a tactile coordinate measuring machine. Fabricating or purchasing a phantom as well as the calibration can be expensive.

Second, care has to be taken to avoid or exclude overlapping spheres and to assign the correct sphere to the corresponding sphere projection in the x-ray images. This typically requires increased efforts regarding the image processing. Kang *et al* [13] addressed this problem by using uniquely identifiable collinear markers.

Third, as a calibration scan with a trajectory identical to the measurement scans is needed, the calibration is comparably time consuming and must be repeated if the scan trajectory is modified.

All three mentioned problems can be avoided if a calibration procedure is established with only one spherical marker, which could be at the expense of the achievable accuracy. Blumensath *et al* [14] presented a calibration method that uses one or several markers with unknown position. They used a multi-step optimization approach to find the intrinsic parameters of the CT scanner as well as the alignment of the linear and rotational manipulator axes. A mathematical description based on vector calculus was used in their approach. The calibration method however was not used for CT measurement tasks, but applied and investigated for nondestructive testing by means of computed laminography [15, 16].

In the following, we present a calibration procedure using a single sphere, but with a slightly different optimization approach that can be performed in a single step and is based on a mathematical description using projection matrices. The principle is to determine the placement of the additional manipulator (i.e. to determine the hexapod base coordinate system) with regard to the CT machine coordinate system (defined by the rotation axis and principal ray). This is done by setting various positions and orientation angles to the hexapod and automatically tracking the corresponding sphere position in the x-ray images. While keeping the intrinsic parameters of the CT device such as the source-detector-distance or

the source-rotation axis-distance fixed (using the outcome of the manufacturer's internal calibration procedure), the six geometric parameters of the pose of the hexapod base coordinate system are then optimized, minimizing the reprojection error between the estimated and measured detector coordinates of the projected sphere center point. Once the hexapod base coordinate system is found by the calibration method, the geometry of any 3D scan trajectory can be calculated in form of projection matrices and fed to the reconstruction software. This enables the algebraic volume reconstruction of CT scans with adaptive tilting of the measurement object.

It is important to note that in our approach, the required intrinsic geometry parameters of the CT device itself are not calibrated but used as prior information. For metrological CT devices that are routinely calibrated, these parameters are typically available with high accuracy. This prior information has already been used in [8]. It has been stated there that this led to more reliable results than calibrating the complete geometry parameter set of the combined system of CT device and additional object manipulator system.

In former work at our institute, a pose sequence applied by a hexapod has already successfully been used for camera calibration and sensor registration for an optical fringe measurement system [17].

The CT calibration method presented here will be validated by means of simulation-based and experimental investigations. Furthermore, the influence of the calibration method not only on the reconstructed volume data but also on dimensional measurement results for 3D scan trajectories is analyzed and discussed. This allows for a judgment if the method is principally feasible for metrological tasks in terms of conformity assessment with respect to the geometric product specification.

In the following section 2, we describe the used setup of cone-beam CT scanner combined with the hexapod as manipulator system. The concatenation of coordinate systems that enables the calculation of projection matrices for different combinations of the scan angle and the hexapod pose is outlined in section 3. The calibration procedure is presented in section 4. In section 5, the method is validated in terms of achievable accuracy and repeatability. The influence of the calibration on dimensional measurements obtained with 3D scan trajectories follows in section 6.

2. System setup and geometry definition

The combined setup of cone-beam CT scanner and hexapod is shown in figure 1. The hexapod H-840.G2 (Physik Instrumente (PI) GmbH & Co. KG, Karlsruhe, Germany) is mounted on top of the rotary table of the CT system Metrotom 1500 G2 (Carl Zeiss Industrielle Messtechnik GmbH, Oberkochen, Germany). The rotary table itself is mounted on a linear axis, enabling different magnifications. The x-ray tube and detector are mounted on a fixed frame. The source-detector-distance is therefore constant. The pose of the hexapod top plate can be set by three position values and three rotation angles. The supplier specifies the repeatability with typical limits of $\pm 0.5 \mu\text{m}$ and $\pm 12 \mu\text{rad}$. More details about the setup can be found in [8]. A 3D scan trajectory for a measurement scan can be achieved

by combining the rotation of the rotary table with scan angle α with a translation and/or rotation of the hexapod top plate.

Following right-handed coordinate systems were defined (also see figure 1(b)), which are later used in sections 3 and 4: the source coordinate system \mathcal{S} is located at the x-ray spot of the tube. The orientation of \mathcal{S} is chosen according to a wide-spread convention. The z-axis is pointing towards the piercing point (point where x-rays hit the detector with right angle). The x- and y-axis are aligned with the detector columns/rows. The world coordinate system \mathcal{W} is located at the crossing of the central ray (from source to piercing point) with the rotation axis of the rotary table (assumed to be ideally aligned). The orientation was chosen in a way to match the one from the later used reconstruction software. While \mathcal{W} stays fixed in space, the coordinate system \mathcal{T} follows the rotation of the rotary table. It is defined in a way that it coincides with \mathcal{W} for a scan angle $\alpha = 0$. Regarding the hexapod, a base coordinate system \mathcal{H} is defined at the zero position of the device. For the orientation, the inherent axes of the device are used. The location of the origin is defined by a set Pivot point, which is adjusted to the respective measurement task. Once set, the coordinate system \mathcal{H} is fixed with regard to the bottom plate of the hexapod.

A second coordinate system $\tilde{\mathcal{H}}$ initially coincides with \mathcal{H} , but follows the transformation of the hexapod top plate (see figure 2). $\tilde{\mathcal{H}}$ is therefore fixed with regard to the top plate. Finally, the 2D detector coordinate system \mathcal{D} has its origin at the center of the bottom left pixel with u - and v -axis aligned with the pixel grid. In contrast to the 3D coordinate systems, the coordinates u and v are dimensionless numbers representing multiples of the pixel side length.

3. Projection matrix calculation for hexapod CT scans

The goal is to use a 6-DOF manipulator e.g. for adaptive tilting of the measurement object during a CT scan. This leads to a 3D scan trajectory, which must be taken into account for a proper reconstruction. The reconstruction software that we use requires information about the 3D scan trajectory in form of projection matrices. In the following, we outline how these projection matrices can be calculated, using the prior information of the CT device and the unknown parameters that will be obtained using the calibration method in section 4.

For the theoretical background about projection matrices, see e.g. [10]. In summary, by projection matrix multiplication, the projection of a 3D point onto the detector (2D coordinates in \mathcal{D}) can be calculated. In our case, we are interested in projection matrices that connect the points of the measurement object in its initial pose in \mathcal{W} (with scan angle $\alpha = 0$ and zero position of the hexapod) to the projected points in the x-ray images. Using such projection matrices, the location and orientation of the volume pixel (voxel) grid after volume reconstruction is identical to the one that is generated by the used reconstruction software (see section 6.2) for a circular trajectory. This allows a direct comparison of the results without registration.

Before we proceed with the concatenation of the introduced coordinate systems to derive the projection matrix formula

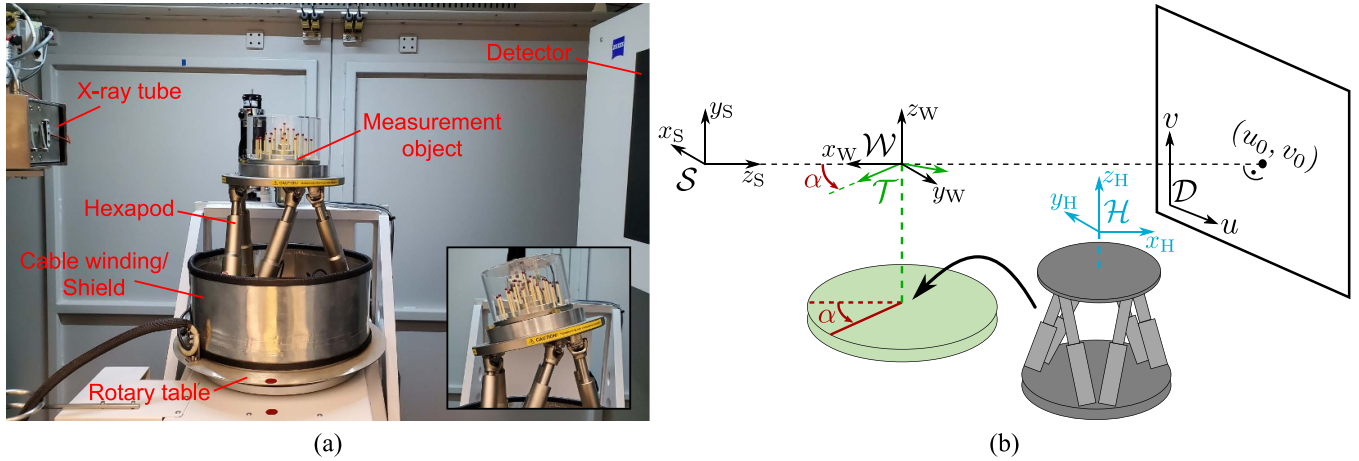


Figure 1. (a) Combined setup of cone-beam CT device and hexapod as object manipulator (small inset: In tilted state). (b) Sketch of the setup with used coordinate systems. α is the scan angle of the rotary table (green).

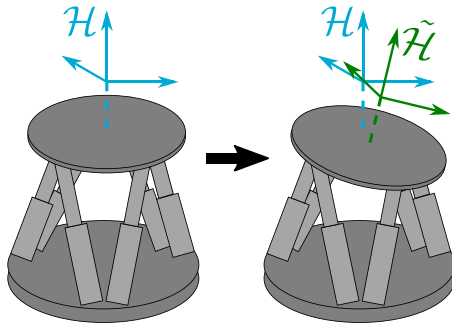


Figure 2. Coordinate systems relating to the hexapod. \mathcal{H} : base coordinate system (defined by axes inherent to the hexapod and the set Pivot point as origin), spatially fixed with regard to the bottom plate. $\tilde{\mathcal{H}}$: moved tool coordinate system after transformation of the top plate, spatially fixed with regard to the top plate. $\tilde{\mathcal{H}}$ coincides with \mathcal{H} if the hexapod is at the zero position.

for the investigated system, some remarks on the mathematical notation should be given. Positions and shifts are given as 3D column vectors (except for the detector coordinate system, where 2D vectors are used). Small, bold italic characters are used for vectors, with subscript indicating the coordinate system the vector belongs to. A circumflex is used if the vector is expressed in homogeneous coordinates, e.g. $\hat{x}_W = (x_W^T, 1)^T$. A transformation between coordinate systems (see also figure 3) is achieved by a 4×4 transformation matrix T . For a vector that is given in a coordinate system \mathcal{A} , the coordinates in \mathcal{B} are obtained by

$$\hat{x}_B = T_{AB} \hat{x}_A = \begin{bmatrix} R_{AB} & t_{AB} \\ \mathbf{0}^T & 1 \end{bmatrix} \hat{x}_A = \begin{bmatrix} R_{AB}^{1,1} & R_{AB}^{1,2} & R_{AB}^{1,3} & t_{AB}^{(1)} \\ R_{AB}^{2,1} & R_{AB}^{2,2} & R_{AB}^{2,3} & t_{AB}^{(2)} \\ R_{AB}^{3,1} & R_{AB}^{3,2} & R_{AB}^{3,3} & t_{AB}^{(3)} \\ 0 & 0 & 0 & 1 \end{bmatrix} \begin{pmatrix} x_A \\ y_A \\ z_A \\ 1 \end{pmatrix}. \quad (1)$$

In this equation, t_{AB} is the shift between the coordinate systems, i.e. the position of the origin of \mathcal{A} in the coordinate system \mathcal{B} . R_{AB} is the extrinsic rotation matrix describing the

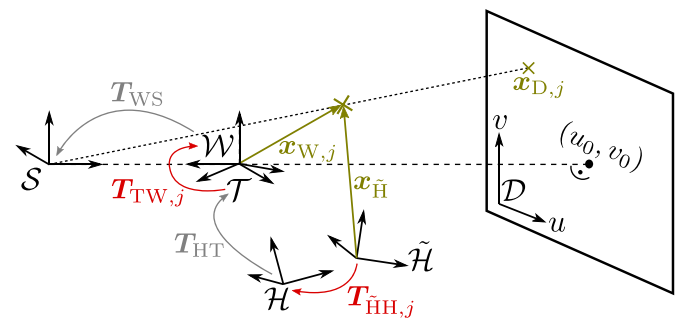


Figure 3. Concatenation of coordinate systems used for the projection matrix calculation for a measurement scan. While the location of a point of the measurement object is constant with regard to the hexapod top plate ($x_{\tilde{H}}$), its location in the world coordinate system ($x_{W,j}$) depends on the varying transformations ($T_{TW,j}$ and $T_{\tilde{H}H,j}$, marked red) during the scan, set by the scan angle of the rotary table and the hexapod pose for the j th projection.

orientational relation between the coordinate systems. See appendix for the definition and the choice of the specific rotation order we used throughout our investigations. The symbols φ_x , φ_y and φ_z are used for rotation angles defining an orientation in the following.

For the example of equation (1), the inverse coordinate transformation is

$$\hat{x}_A = T_{AB}^{-1} \hat{x}_B = \begin{bmatrix} R_{AB}^{-1} & -R_{AB}^{-1} t_{AB} \\ \mathbf{0}^T & 1 \end{bmatrix} \hat{x}_B,$$

where the inverse of the rotation matrix R_{AB}^{-1} is identical to its transposed R_{AB}^T .

To be able to identify vectors or transformations in a sequence of different poses, indices are appended in some cases as second subscript to indicate the pose number. For the scan trajectory of a measurement scan, we use j , while k is used for the transformation sequence applied for the calibration procedure.

Using the introduced notation and considering the combined movement by chaining the coordinate systems as indicated in figure 3, a formula can be derived to determine where a point of the measurement object is projected on the detector for

different poses of the measurement scan, i.e. for different scan angles of the rotary table and poses of the hexapod. In figure 3, transformations that are constant during a scan (T_{WS}, T_{HT}) are colored light gray and transformations that change for each pose ($T_{TW,j}, T_{HH,j}$) are colored red.

A cone-beam projection is generally expressed by a 3×4 projection matrix P . For coordinates in the source coordinate system \mathcal{S} , the projection matrix P_S is only composed of an intrinsic 3×3 matrix K , which is termed camera calibration matrix in optics, and the zero vector. For our definition of the orientations of \mathcal{S} and \mathcal{D} from figure 1(b), we obtain

$$\hat{x}_{D,j} = P_S \hat{x}_{S,j} = [K|0] \hat{x}_{S,j} = \begin{bmatrix} -\frac{d_{SD}}{p_u} & 0 & u_0 & 0 \\ 0 & \frac{d_{SD}}{p_v} & v_0 & 0 \\ 0 & 0 & 1 & 0 \end{bmatrix} \hat{x}_{S,j}. \quad (2)$$

In this equation, d_{SD} is the source-detector-distance, (p_u, p_v) is the pixel pitch (pixel side length) in u - and v -direction, and $(u_0, v_0)^T$ are the coordinates of the piercing point in \mathcal{D} . \hat{x}_D is a 3D homogeneous vector, where the 2D detector coordinates $(u, v)^T$ can be derived from the relation $\hat{x}_D = (uw, vw, w)^T$. For equation (2), $w = z_S$, but in general, w is a scaling factor obtained from projection matrix multiplication that is needed for the calculation of the 2D coordinates from the homogeneous coordinates.

For the projection formula (2), we need the position of the 3D points of the measurement volume in \mathcal{S} . The measurement volume is moved during the scan with regard to \mathcal{S} , but is fixed with regard to $\tilde{\mathcal{H}}$. Therefore, we can link the coordinate systems to get a mapping $\hat{x}_{\tilde{\mathcal{H}}} \rightarrow \hat{x}_{D,j}$:

$$\hat{x}_{D,j} = P_S \hat{x}_{S,j} = P_S T_{WS} T_{TW,j} T_{HT} T_{HH,j} \hat{x}_{\tilde{\mathcal{H}}} = P_j \hat{x}_{\tilde{\mathcal{H}}}. \quad (3)$$

The transformation matrix T_{WS} only depends on the distance between the x-ray source and the rotation axis d_{SR} , which is taken from the output of the internal calibration procedure of the CT device. From figure 1(b), it can be derived that

$$T_{WS} = \begin{bmatrix} 0 & -1 & 0 & 0 \\ 0 & 0 & 1 & 0 \\ -1 & 0 & 0 & d_{SR} \\ 0 & 0 & 0 & 1 \end{bmatrix}. \quad (4)$$

The transformation due to the rotary table $T_{TW,j}$ only consists of a rotation around the z -axis and is therefore

$$T_{TW,j} = \begin{bmatrix} R_z(\alpha_j) & \mathbf{0} \\ \mathbf{0}^T & 1 \end{bmatrix}.$$

For our investigations, we use homogeneously increasing scan angles $\alpha_j = (j-1) \cdot 2\pi/n$ with $j \in [1, n]$, where n is the number of projections for the scan. The transformation T_{HT} depends on how the hexapod has been mounted and adjusted on the rotary table. It is constant during the scan, but only roughly known. For metrological purposes, however, the matrix entries must be accurately known. The matrix (or rather

the three rotation angles and three components of the shift) is therefore determined by the calibration procedure that is presented in the next section 4. Finally, $T_{HH,j}$ is calculated according to equation (1) using the position values and rotation angles set to the hexapod.

As already mentioned, the goal is a representation of the measurement volume in \mathcal{W} in the initial state (zero scan angle and hexapod in zero position/orientation). We indicate this state with $j=0$. Consequently, a mapping $\hat{x}_{W,0} \rightarrow \hat{x}_{D,j}$ is required. This can be achieved by expressing $\hat{x}_{\tilde{\mathcal{H}}}$ as $\hat{x}_{\tilde{\mathcal{H}}}(\hat{x}_{W,0})$. To reach this, we use

$$\hat{x}_{W,0} = T_{TW,0} T_{HT} T_{HH,0} \hat{x}_{\tilde{\mathcal{H}}} = I T_{HT} \hat{x}_{\tilde{\mathcal{H}}} = T_{HT} \hat{x}_{\tilde{\mathcal{H}}},$$

where I is the 4×4 identity matrix. The expression can be rearranged to

$$\hat{x}_{\tilde{\mathcal{H}}} = T_{HT}^{-1} \hat{x}_{W,0}$$

and inserted back into equation (3):

$$\hat{x}_{D,j} = P_S T_{WS} T_{TW,j} T_{HT} T_{HH,j} T_{HT}^{-1} \hat{x}_{W,0} = P_j \hat{x}_{W,0}. \quad (5)$$

P_j in equation (5) is the projection matrix that is finally fed to the reconstruction software for each projection. The only unknown in the equation for P_j is T_{HT} , which is determined by the calibration procedure presented in the next section.

4. Single sphere calibration method

To obtain the transformation T_{HT} , which is needed for the computation of the projection matrices for a 3D scan trajectory, a ball is mounted on the top plate of the hexapod and imaged at different poses of the hexapod. Setting up a formula that describes the locations of the projected sphere midpoint gives then the possibility to optimize the parameters of T_{HT} by minimizing the reprojection error (difference between measured and calculated detector coordinates).

Before we give more information about the used sequence of poses and the method for detecting the projected sphere midpoint in the x-ray images, we first derive the formula for the reprojection error, which is used as objective function in the optimization step. The formula for the calculated detector coordinate can be derived with the help of figure 4. The concatenation of coordinate systems is the same as presented in the previous section, with the difference that the rotary table is not used for the calibration procedure. Therefore, T_{TW} is the identity matrix $T_{TW} = I$ and \mathcal{T} coincides with \mathcal{W} . The calibration procedure consists of performing a sequence of specific hexapod poses, expressed by $T_{HH,k}$. To be able to calculate the coordinates of the projected midpoint $x_{D,k} = (u_k, v_k)^T$ for each projection of the calibration procedure, besides the unknown T_{HT} , the position t of the sphere in the moved coordinate system of the hexapod is needed. t could potentially be determined with additional measuring systems, but as one purpose of our method is to be independent of further measurement devices, t is treated unknown and has therefore also been determined by the

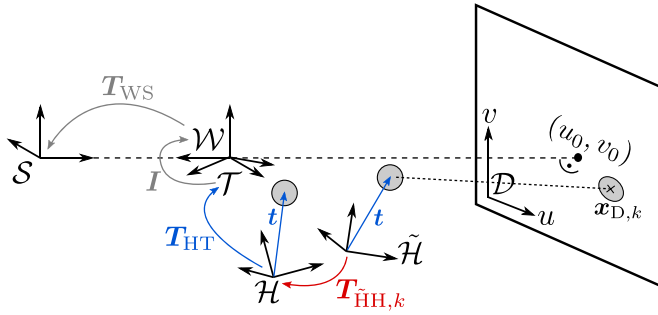


Figure 4. Concatenation of coordinate systems used for the calibration procedure. The rotary table is held constant at $\alpha = 0$ (leading to $T_{TW} = I$). The hexapod moves to different poses $T_{HH,k}$. The constant but unknown parameters T_{HT} and t are determined by optimization, using the projected midpoints of the sphere.

optimization process. In sum, following projection formula is obtained:

$$\hat{x}_{D,k} = P_S T_{WS} T_{HT} T_{HH,k} \begin{pmatrix} t \\ 1 \end{pmatrix}. \quad (6)$$

If the detector coordinates of the midpoint projection are measured by means of image processing, the unknowns T_{HT} and t can be optimized, minimizing the squared distances d_k^2 between the measured points $x_{D,k,\text{meas}}$ and the calculated ones from equation (6):

$$\begin{aligned} \theta_{\text{opt}} &= \arg \min_{\theta} \sum_k d_k^2(\theta) \\ &= \arg \min_{\theta} \sum_k \|x_{D,k,\text{meas}} - x_{D,k}(\theta)\|_2^2. \end{aligned} \quad (7)$$

In θ , the overall nine parameters of T_{HT} and t are subsumed:

$$\theta = \left(\varphi_{HT,x}, \varphi_{HT,y}, \varphi_{HT,z}, t_{HT}^{(1)}, t_{HT}^{(2)}, t_{HT}^{(3)}, t^{(1)}, t^{(2)}, t^{(3)} \right).$$

For the optimization, we used the nonlinear least squares solver based on the Levenberg–Marquardt algorithm from the optimization toolbox of Matlab R2020b. This toolbox allows an easy implementation directly based on equations (6) and (7) without the need for advanced knowledge in the field of mathematical optimization. The only adaption we made was to change the default abort criteria to ensure that a further increase of the computational effort would only lead to negligible changes in the resulting values of θ . The used source code is provided as supplementary data to this article.

A reasonable starting point should be applied for the optimization. We used a rough estimate based on the orientation of the clamping (see figure 1(b)) and the fact that the Pivot point was roughly set to the position of the sphere, which is projected near the center of the image. Thus, θ was initialized with $(0, 0, \pi, 0, 0, 0, 0, 0, 0)$.

For the calibration procedure, different pose sequences of the hexapod can generally be chosen. The pose sequences that we used for the validation of the method and for the reconstruction of 3D trajectories are presented in the next section.

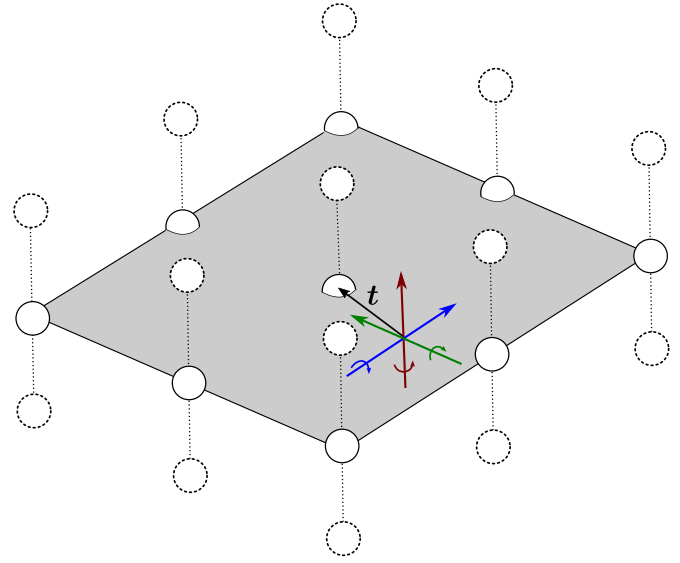


Figure 5. Position grid as basis for the generation of the pose sequence for the hexapod. At each position, the sphere is rotated around each single axis of the hexapod.

5. Validation

We performed the calibration procedure experimentally with the setup presented in section 2 as well as by means of radiographic simulations with geometry settings adapted to the experiments.

In each case, the pose sequences that we investigated are based on a grid of positions (see figure 5). The grid spacing is homogeneous with maximum/minimum position values of ± 10 mm for each axis. For each position, the sphere is imaged first without rotation and then with a rotation of $\pm 5^\circ$ around each axis separately. This results in seven projection images per position.

In case of experiments, a metal ball made from tungsten carbide with a diameter of 8 mm and a grade G10 according to DIN 5401 [18] was used. The ball has been pressed inside a hollow cylindrical sample holder made from polyether ether ketone, which is mounted on the hexapod top plate with different cylindrical extensions (see figure 6). For experiments, we used a grid of 3×3 positions. This results in sum in 189 projections. Exemplary x-ray images of the resulting sequence are shown in figure 6(c).

The calibration procedure has been performed at two different magnifications (2.7 and 5.3), which were tailored to the measurement tasks presented in section 6. For each magnification, the procedure was experimentally performed twice to be able to investigate the repeatability. As input for the optimization, the read out values from the encoders of the hexapod were used for the parameters of $T_{HH,k}$.

We replicated the experimental calibration procedures with simulated x-ray images using the software aRTist 2.12 (BAM Federal Institute for Materials Research and Testing, Berlin, Germany). The simulations were performed with settings (geometry, tube and detector properties) that have been adjusted to the used CT device. The expansion of the x-ray spot,

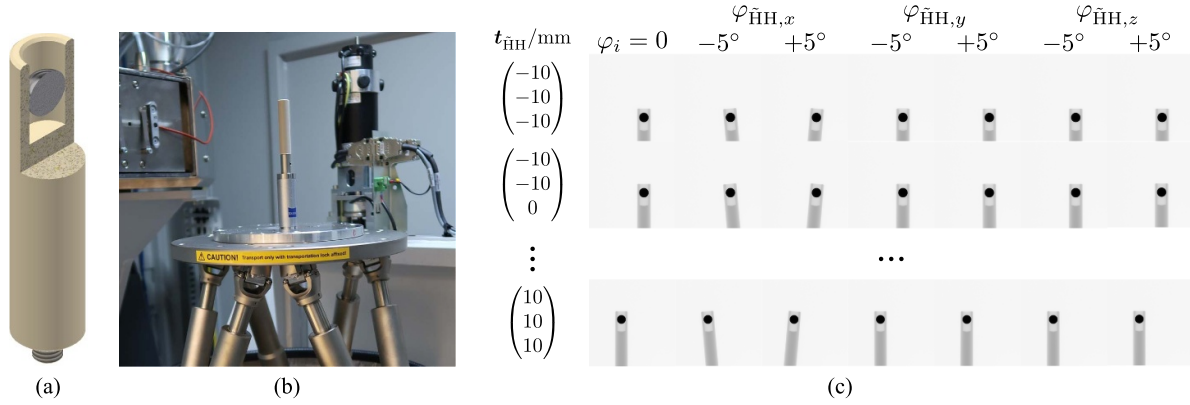


Figure 6. Experimental realization of the calibration procedure. (a) Schematic of the pressed-in metal ball inside the sample holder. (b) Mounted sample holder. (c) Exemplary x-ray images for the pose sequence.

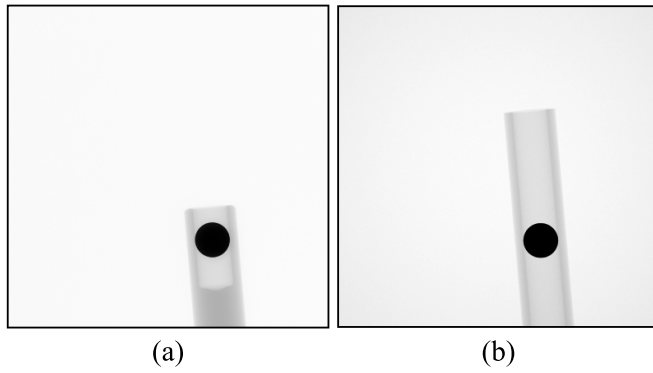


Figure 7. Exemplary x-ray image of the calibration procedure obtained by experiment (a) and simulation (b). The gray values are linearly scaled between the minimum (black) and the maximum (white) intensity value, respectively. As only the edge region of the ball is relevant, for simplification reasons, the sample holder geometry was not completely adjusted to the real part.

the polychromatic source spectrum and the noise as well as unsharpness of the detector were considered. The sample holder was replaced by a tube as simplified geometry in the simulation. The pose sequence of the hexapod was virtually performed based on programmed scripts using the Tcl interface of the software. The geometric parameters T_{HT} and t were roughly set to the outcome of the experimental results. The positioning of the hexapod was simulated without deviations from the ideal theoretical poses. An exemplary simulated x-ray image is shown in figure 7 in comparison to the corresponding experimentally obtained image.

In case of simulations, we investigated different grid sizes for the positions from $2 \times 2 \times 2$ to $5 \times 5 \times 5$. As the position of the sphere and the coordinate system of the hexapod are exactly known in the simulation, the accuracy of the calibration method can be directly evaluated.

The image processing steps to detect the projected sphere midpoints in the x-ray images were the same for experiment and simulation and identical to the method used in our former publication [8]. Thus, the midpoint of the ellipse fitted to the edge of the sphere projection was determined and corrected according to [19].

5.1. Simulation results

Before the calibration procedure was virtually performed, we tested the optimization algorithm by feeding in the theoretical exact 2D coordinates instead of the measured coordinates. Doing so, the optimization yielded the exact values for θ . This proves that the algorithm converges in principle to the correct solution for the investigated pose sequences.

Simulating the complete calibration procedure including the x-ray imaging and sphere detection leads to deviations between measured and calculated 2D coordinates, which in turn leads to inaccurate end results for the optimization process. Table 1 lists the resulting deviations for the two investigated magnifications and the different number of poses.

The table contains the root mean square (rms) value of the distances between the detected and calculated (according to equation (5) using the optimized T_{HT}) 2D coordinates:

$$d_{\text{rms}}^{\text{opt}} = \sqrt{\frac{1}{n} \sum_k d_k^2} = \sqrt{\frac{1}{n} \sum_k \|\mathbf{x}_{\text{D},k,\text{meas}} - \mathbf{x}_{\text{D},k}(\theta_{\text{opt}})\|_2^2}. \quad (8)$$

We term this measure reprojection error in the following. It is directly connected to the objective function (7) and can be seen as mean pixel deviation after optimization. However, in case of simulations, we also know the exact value of T_{HT} and can therefore also calculate the theoretically exact 2D coordinates. Therefore, we can also calculate the rms value with regard to the exact coordinates

$$d_{\text{rms}}^{\text{exact}} = \sqrt{\frac{1}{n} \sum_k \|\mathbf{x}_{\text{D},k,\text{meas}} - \mathbf{x}_{\text{D},k}(\theta_{\text{exact}})\|_2^2}, \quad (9)$$

which is a direct measure for the accuracy of the ellipse detection method. From table 1, it can be seen that the accuracy of the ellipse detection is around 1/50 of the pixel side length for the simulated projection images. For the used detector, this corresponds to $4 \mu\text{m}$ in the image plane.

The values $d_{\text{rms}}^{\text{opt}}$ are even slightly below the values of $d_{\text{rms}}^{\text{exact}}$. This is due to the fact that the optimization does not find the

Table 1. Simulation results. Here, $\Delta t_{\text{HT}}^{\text{exact}}$, $\Delta \varphi_{\text{HT}}^{\text{exact}}$ and Δt^{exact} are the deviations from the true values.

Magnification	No. of poses	$d_{\text{rms}}^{\text{opt}}$ (pixels)	$d_{\text{rms}}^{\text{exact}}$ (pixels)	$\Delta t_{\text{HT}}^{\text{exact}}$ (μm)			$\Delta \varphi_{\text{HT}}^{\text{exact}}$ (μrad)			Δt^{exact} (μm)		
				x	y	z	x	y	z	x	y	z
2.7	$2 \times 2 \times 2 \times 7$	0.0200	0.0207	1.9	3.4	1.8	-6.1	14.0	2.2	3.3	3.4	-2.0
2.7	$3 \times 3 \times 3 \times 7$	0.0214	0.0219	13.8	1.8	0.6	-3.5	1.4	5.6	1.2	1.7	-0.7
2.7	$5 \times 5 \times 5 \times 7$	0.0243	0.0244	-1.9	-1.3	-1.7	-2.9	-4.3	-7.1	-0.6	-1.3	1.7
5.3	$2 \times 2 \times 2 \times 7$	0.0194	0.0198	1.18	0.7	-0.1	3.0	7.4	3.3	1.1	0.8	0.1
5.3	$3 \times 3 \times 3 \times 7$	0.0207	0.0209	-0.05	0.1	0.8	3.0	6.4	-2.6	-0.4	0.1	-0.7
5.3	$5 \times 5 \times 5 \times 7$	0.0208	0.0209	-0.02	0.2	0.4	-0.5	8.8	-0.6	0.4	0.3	-0.4

Table 2. Experimental results. Here, Δt_{HT} , $\Delta \varphi_{\text{HT}}$ and Δt are the differences between the outcome from the two single calibration runs.

Magnification	Run	No. of poses	$d_{\text{rms}}^{\text{opt}}$ (pixels)	Δt_{HT} (μm)			$\Delta \varphi_{\text{HT}}$ (μrad)			Δt (μm)		
				x	y	z	x	y	z	x	y	z
2.7	1	$3 \times 3 \times 3 \times 7$	0.1578									
2.7	2	$3 \times 3 \times 3 \times 7$	0.1542	-11.9	-10.8	-11.8	-4.3	87.5	-156.2	312.6	-97.7	9.6
5.3	1	$3 \times 3 \times 3 \times 7$	0.4960									
5.3	2	$3 \times 3 \times 3 \times 7$	0.4947	-7.4	1.0	0.4	-5.0	24.7	24.7	2.2	-4.5	-0.9

true values θ_{exact} (compare the deviations given in table 1), but alternative values that compensate for the inaccuracies of the ellipse detection and lead to a lower value for the objective function than the true values. It can therefore be inferred that the optimization algorithm works correctly in terms of minimizing the objective function and that the resulting deviations are mainly caused by the finite pixel size and image noise.

As an interesting detail, it can be observed that the deviations $\Delta t_{\text{HT}}^{\text{exact}}$ and Δt^{exact} are not independent. In fact, the deviations nearly compensate for each other. Looking for example at the z component, the values for Δt^{exact} are very accurate the negative values of the z component of $\Delta t_{\text{HT}}^{\text{exact}}$. In case of the x and y components one must consider that the coordinate systems, in which t_{HT} and t are defined, are oriented towards each other by an 180° rotation around the z -axis. Thus, a compensation is expressed by identical values (instead of negative values). For the y component, this can be confirmed while for the x component larger differences exist. This is attributed to the fact that the sensitivity of the position of the projection is lower for a shift of the sphere in direction of the optical axis (x -direction) in comparison to a shift in the image plane. For a possible improvement of the method, in future, the rotary axis of the CT device could be used to capture calibration images also at a scan angle of 90° . Doing so, the hexapod translations for calibration could be restricted to movements that are perpendicular to the optical axis for the respective scan angle.

5.2. Experimental results

In case of experiments, the true values for T_{HT} are not known. Therefore, $d_{\text{rms}}^{\text{exact}}$ and the deviations of the geometric parameters with regard to the true values cannot be determined. However, the reprojection error after optimization $d_{\text{rms}}^{\text{opt}}$ still gives a hint on the accuracy. Furthermore, the differences between the results of the respective two different calibration runs allow for

an rough estimation of the repeatability. The according values can be found in table 2.

Regarding the reprojection error $d_{\text{rms}}^{\text{opt}}$, the relative difference between the repetitions of the calibration procedure are 2% or less. However, the values are one order of magnitude larger than the results from simulation in table 1. A closer look on the pose-wise distances between detected and calculated 2D coordinates d_k (see equation (8) for the definition of d_k) allows for analyzing the reasons for the comparatively large reprojection error. The values of d_k for one exemplary calibration run are plotted in figure 8 in comparison to the values obtained by simulation.

In case of the simulation, the values of d_k are homogeneously distributed for the pose sequence. In contrast, the values from experiment show distinct large values above 0.8 for specific poses. A comparison with figure 6 yields that these high values belong to poses with $\varphi_{\text{HH},y} = \pm 5^\circ$, i.e. when a rotation around the hexapod y -axis is applied. Contrary, for the poses with no rotation ($\varphi_i = 0$), the values for d_k are between 0.003 and 0.05 with a rms value of 0.031 and are therefore in a similar range in comparison to the simulation. For rotations around the x - and z -axis, the rms value is 0.069 and 0.144, respectively. For a magnification of 2.7, the characteristic behavior is the same (not shown here). It is therefore assumed that the calibration procedure including the image processing works in principle correctly for the experimental case and that the overall large reprojection error is mainly caused by inaccuracies of the y tilting of the hexapod. To examine the influence of the orientation used for the mounting of the hexapod ($\varphi_{\text{HT}} \approx (0, 0, \pi)$), we repeated the experiment at a later time with the rotary table positioned at $\alpha = 90^\circ$. The diagram for the reprojection error (not shown here) was similar to figure 8(b), but now with high d_k values for rotations around the hexapod x -axis. This suggests that there exist similar inaccuracies of the hexapod for x as well as y tilting, but the sensitivity of the projected position on those errors is different for the two axes.

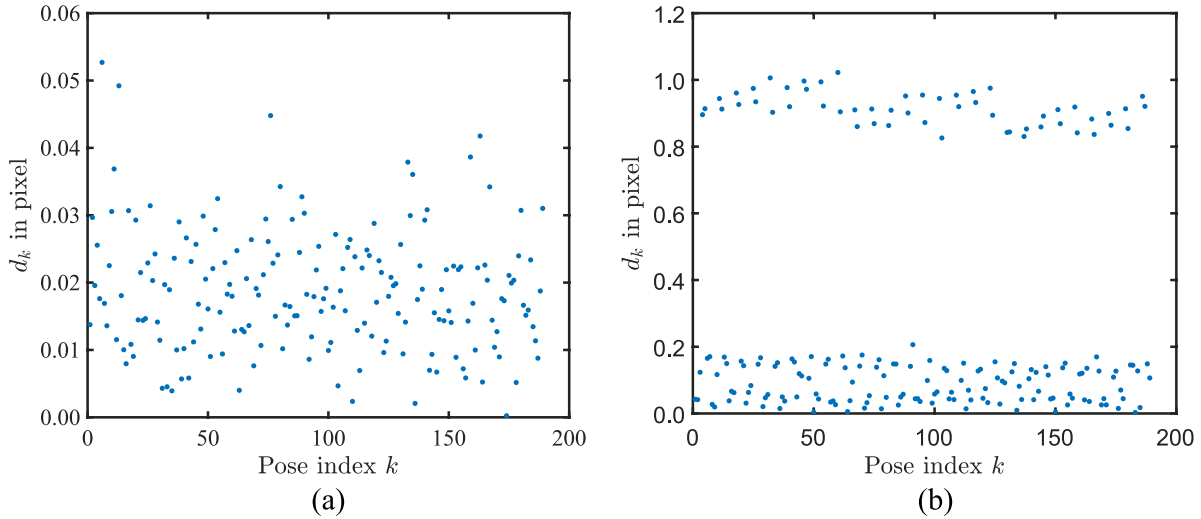


Figure 8. Reprojection error for each pose of the calibration procedure for simulation (a) and experiment (b) at a magnification of 5.3.

The deviations between the geometric parameters obtained from the two different calibrations runs, respectively, (see Δt_{HT} , $\Delta \varphi_{HT}$ and Δt in table 2) are higher than the absolute deviations from the true values for the simulations. While the repeatability therefore seems to be quite low for the application of the calibration method for dimensional measurement tasks with CT, it has to be considered that deviations for t_{HT} and φ_{HT} are not to be put on a level with dimensional errors for measurands in a CT scan, which will also become clear from the results in the next section.

6. Application on metrological CT scans with 3D scan trajectories

As already mentioned, in the experimental case, the absolute deviations for the resulting geometric parameters cannot be determined as the reference values are not known. Therefore, we performed 3D scan trajectories for two different measurement objects and the two investigated magnifications to evaluate the influence of the calibration procedure on the resulting accuracy for dimensional measurements in comparison to the standard circular scan trajectory, which was also applied. In this way, a direct statement about the feasibility of the method for metrological CT can be made. The repetitions of the calibration runs presented in the last section were furthermore conducted before and after each measurement scan. Therefore, the repeatability can also be discussed in terms of dimensional measurement errors.

6.1. Measurement objects and scan trajectories

Figure 9 gives an overview of the used measurement objects and scan trajectories that we used for the metrological CT scans.

The 3D scan trajectories are generated by applying a tilt for the hexapod top plate, while the position values $t_{HH,j}$ are kept constant at zero. The specific shapes of the trajectories have no physical background, i.e. they were not adjusted to

the object geometries in any way and only represent possible regular shapes that were exemplary chosen.

In the following, we describe the calculation of the angles that should be set to the hexapod to obtain the desired trajectory shapes. As certain approximations will be used, it is important to note that these calculations are not used for the computation of the projection matrices for the reconstruction, but only to implement the scan trajectories for the measurement scan.

The trajectory shapes in figure 9 can generally be achieved by a tilt around the y_W -axis (see figure 1(b)). This means that the measurement object is always tilted around an horizontal axis that is perpendicular to the central ray and is therefore fixed with regard to the x-ray source and the detector. To obtain such a tilt, it has to be considered that the hexapod is moved with the rotary table. Mathematically, this means that the hexapod top plate is rotated first and then the rotary table is rotated. The resulting orientation of the hexapod top plate must be identical to the one that would be obtained if the rotary table was rotated first and then the hexapod top plate was tilted by $\varphi_{\text{tilt},j}$ around the y_W -axis. This can be expressed by

$$\mathbf{R}_{TW,j} \mathbf{R}_{HT} \mathbf{R}_{HH,j} = \mathbf{R}_{y,j}(\varphi_{\text{tilt},j}) \mathbf{R}_{TW,j} \mathbf{R}_{HT}.$$

Strictly speaking, the tilt $\mathbf{R}_{y,j}(\varphi_{\text{tilt},j})$ is only exactly around the y_W -axis, if besides from $t_{TW,j} = t_{HH,j} = \mathbf{0}$, also $t_{HT} = \mathbf{0}$ (see figure 3). Due to the realized mounting of the hexapod and the set Pivot point, the origin of \mathcal{H} is close to the origin of \mathcal{W} (in the order of some mm) and therefore the approximation $t_{HT} \approx \mathbf{0}$ is valid for the present purpose.

The roughly needed orientation of the hexapod $\mathbf{R}_{HH,j}^{\text{set}}$ to be set for a specific desired tilt angle $\varphi_{\text{tilt},j}$ can therefore be calculated by

$$\mathbf{R}_{HH,j}^{\text{set}} = \mathbf{R}_{HT}^{-1} \mathbf{R}_{TW,j}^{-1} \mathbf{R}_{y,j}(\varphi_{\text{tilt},j}) \mathbf{R}_{TW,j} \mathbf{R}_{HT}. \quad (10)$$

The extraction of the rotation angles ($\varphi_{HH,x,j}^{\text{set}}$, $\varphi_{HH,y,j}^{\text{set}}$, $\varphi_{HH,z,j}^{\text{set}}$) from the rotation matrix $\mathbf{R}_{HH,j}^{\text{set}}$ is given in [appendix](#).

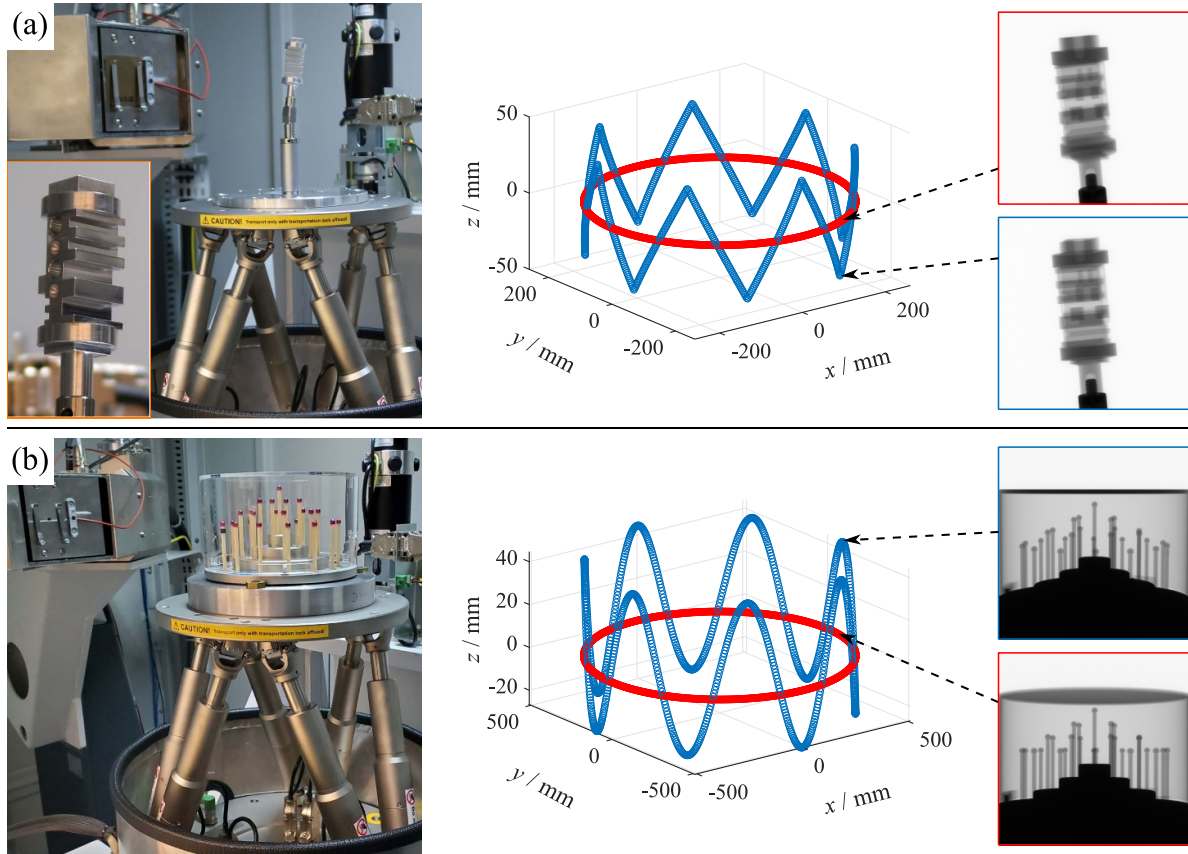


Figure 9. Mounted measurement objects (left column), source trajectory (middle) for 3D scan (blue) and circular scan (red) and exemplary x-ray images (right) for the multi-feature specimen (a) and the multi-sphere length standard.

The results from the calibration procedure were not immediately available at the time of the 3D scans. Therefore we further used the approximation $\mathbf{R}_{HT} \approx \mathbf{R}_z(\pi)$, as the hexapod is mounted very close to this orientation. Again, it is important to note that the approximation for \mathbf{R}_{HT} and equation (10) were only used to calculate the wanted hexapod pose settings ($T_{HH,j}^{set}$). For the calculation of the projection matrices used for reconstruction equation (5), the optimized \mathbf{R}_{HT} from the calibration procedure and the values for $T_{HH,j}$ obtained by the encoder readouts were used.

The first object, termed multi-feature specimen in the following, is made from Aluminum (EN AW-6082) and has already been used in our former work [8]. To obtain a stable fixture, the object was screwed on the hexapod top plate with cylindrical extensions. The object was mounted in an already tilted orientation at zero hexapod position to get a high quality for the circular reference scan (also see investigations about the optimal orientation in [20]). The scan trajectory results from a tilt angle that varies in form of a triangle wave with an amplitude of 8° , a phase shift of 90° and seven periods over the full scan. The exact values in dependence of the scan angle α_j in radian can be expressed in a compact form by

$$\varphi_{\text{tilt},j} = \frac{28}{45} \left| \left(\left(\alpha_j + \frac{\pi}{14} \right) \bmod \left(\frac{2\pi}{7} \right) \right) - \frac{\pi}{7} \right| - \frac{2\pi}{45}, \quad (11)$$

where mod is the modulo function, i.e. $a \bmod m$ is the remainder after division of a by m .

The second object is a calibrated multi-sphere length standard (METROTOM-Check from Carl Zeiss Industrielle Messtechnik GmbH, Oberkochen, Germany) with 27 ruby spheres with diameter of 5 mm on ceramic shafts and a base made from Invar. A special clamping plate was designed for stable mounting of the object on the hexapod top plate. The tilt angle to construct the scan trajectory was varied sinusoidally with an amplitude of 4° and an offset of 1° and seven periods over the full scan. The values in radian are

$$\varphi_{\text{tilt},j} = \frac{\pi}{180} + \frac{4\pi}{180} \sin(7\alpha_j).$$

6.2. Measurement settings and methods

The used CT settings for the scans and for the according calibration runs are listed in table 3. Generally, the calibration procedures were performed with lower tube voltage as the focus here is on a good contrast on the resulting edges of the projected ball and not on a sufficient penetration of the center area. The CT scans were conducted with 2×2 pixel binning to obtain a lower number of voxels for the reconstructed volume. The reason for that is that the voxel number is limited by the memory size of the graphics card used for the iterative reconstruction algorithm.

The reconstruction was performed with a C++ program that makes use of the application programming interface of the software CERA 6 (Siemens Healthcare GmbH, Erlangen,

Table 3. Used parameters for the measurement scans and calibration procedures. The nomenclature for the measurement objects is according to figure 9.

Magnification	2.7		5.3	
	Meas.	Calib.	Meas.	Calib.
Type				
Object	(b)	ball	(a)	ball
Number of projections	1000	189	900	189
X-ray tube voltage (kV)	180	120	180	100
X-ray tube current (μA)	350	600	370	370
Pre-filter (Cu) (mm)	—	—	0.25	—
Integration time (s)	1.0	1.0	1.0	2.0
Images averaged	1	2	1	2
Gain	8	8	8	8
Pixel binning	2×2	1×1	2×2	1×1
Voxel side length (μm)	148.2	—	75.6	—

Germany). The iterative reconstruction based on the simultaneous algebraic reconstruction technique, i.e. the CERA ART pipeline with algorithm setting ‘basic’ was used. For each measurement scan, a single iteration was performed with a relaxation factor of 0.8. The resulting voxel values were exported as floating-point numbers with 32 bit precision. The geometry of the 3D scan trajectories was considered by reading in the projection matrices P_j , which were calculated according to equation (5) using the experimental calibration results for T_{HT} from the previous section and the set hexapod transformations from equation (10).

For both measurement objects, dimensional measurands for which calibration data from tactile coordinate measuring machines (CMMs) exist were investigated. In this way, the measurement errors can directly be assessed. In case of the multi-feature specimen, additionally, a target-actual comparison was performed. All dimensional measurements were evaluated using the software VGStudio Max 3.5 (Volume Graphics GmbH, Heidelberg, Germany). The surfaces of the measurement objects were iteratively extracted using the setting ‘Advanced’ with automatic material detection from the gray level histogram.

The geometry of the multi-feature specimen principally allows for a high number of length measurands. However, it was observed from regularly repeated tactile calibrations that specific, mainly bidirectional, length measurands are prone to fluctuations that are too high in comparison to typical measurement errors of CT measurements to be regarded as proper reference. For this reason, a calibration measurement was performed once with an in-house CMM (UPMC 1200 CARAT S-ACC, Carl Zeiss Industrielle Messtechnik GmbH, Oberkochen, Germany) and second, externally at a service provider with the CMM PRISMO ultra (Carl Zeiss Industrielle Messtechnik GmbH, Oberkochen, Germany). The investigation of measurement errors for CT were then restricted to measurands for which the calibration results between the two tactile measurements differed less than $0.3 \mu\text{m}$. The according measurands are shown in figure 10. The mean of the two single tactile measurements results was used. All measurands are based on geometry

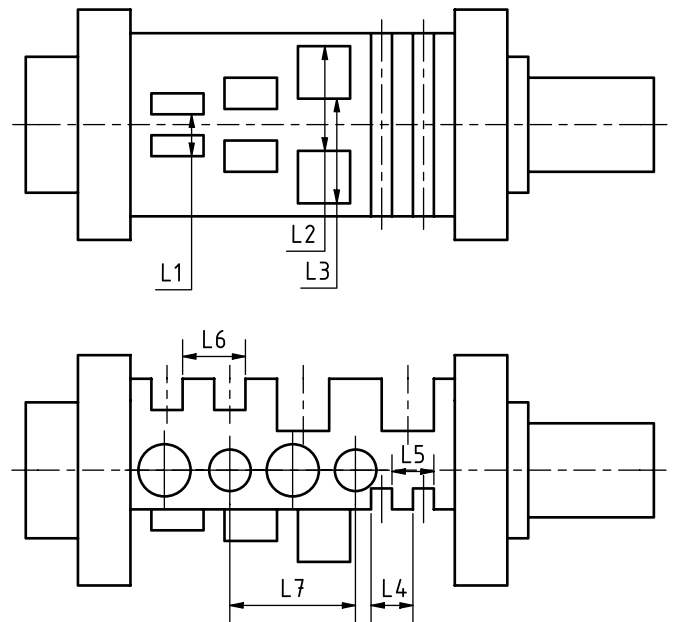


Figure 10. Investigated measurands for the multi-feature specimen. The measurands are distances between planes ($L1$ to $L6$) or calottes ($L7$) and have nominal values between 4 mm and 12 mm. The outer dimension of the specimen is 60 mm along the part axis.

elements that are fitted to the probing points in a least squares sense.

As reference for the target-actual comparison of the multi-feature specimen, not the computer-aided design (CAD) model of the part was used, but a surface triangle mesh derived from the CAD and corrected for manufacturing deviations according to [21]. The necessary reference data for this technique was obtained using the already mentioned tactile in-house CMM. First, the method converts the nominal CAD geometry into a high-fidelity triangle mesh, with a target triangle edge length of approx. $100 \mu\text{m}$, which is independent of the local geometry curvature. Next, the vertices of this mesh are shifted based on the CMM probing points for each geometry element (e.g. cylinder) using Voronoi interpolation. Because of the fact, that it is usually not possible to tactilely probe work piece edges and in order to allow arbitrary CMM probing patterns, the method does not shift edge vertices, which means that edge regions are by design described by the nominal geometry. Therefore, the result is a hybrid nominal/actual high-fidelity triangle mesh, which locally represents the CMM measurement data or the CAD geometry in edge regions and for unprobed geometry elements. The nominal-actual comparison is then at the location of the triangle vertices, which are by design not affected by interpolation error associated with curved regions.

In case of the multi-sphere length standard, the distances between the sphere midpoints as well as the sphere diameters and sphericity values were defined as measurement tasks. While calibration data exist for the distances and diameters, this is not the case for the sphericity. However, for the ruby spheres of the object, deviations from the spherical form due to manufacturing errors are much lower than typical CT

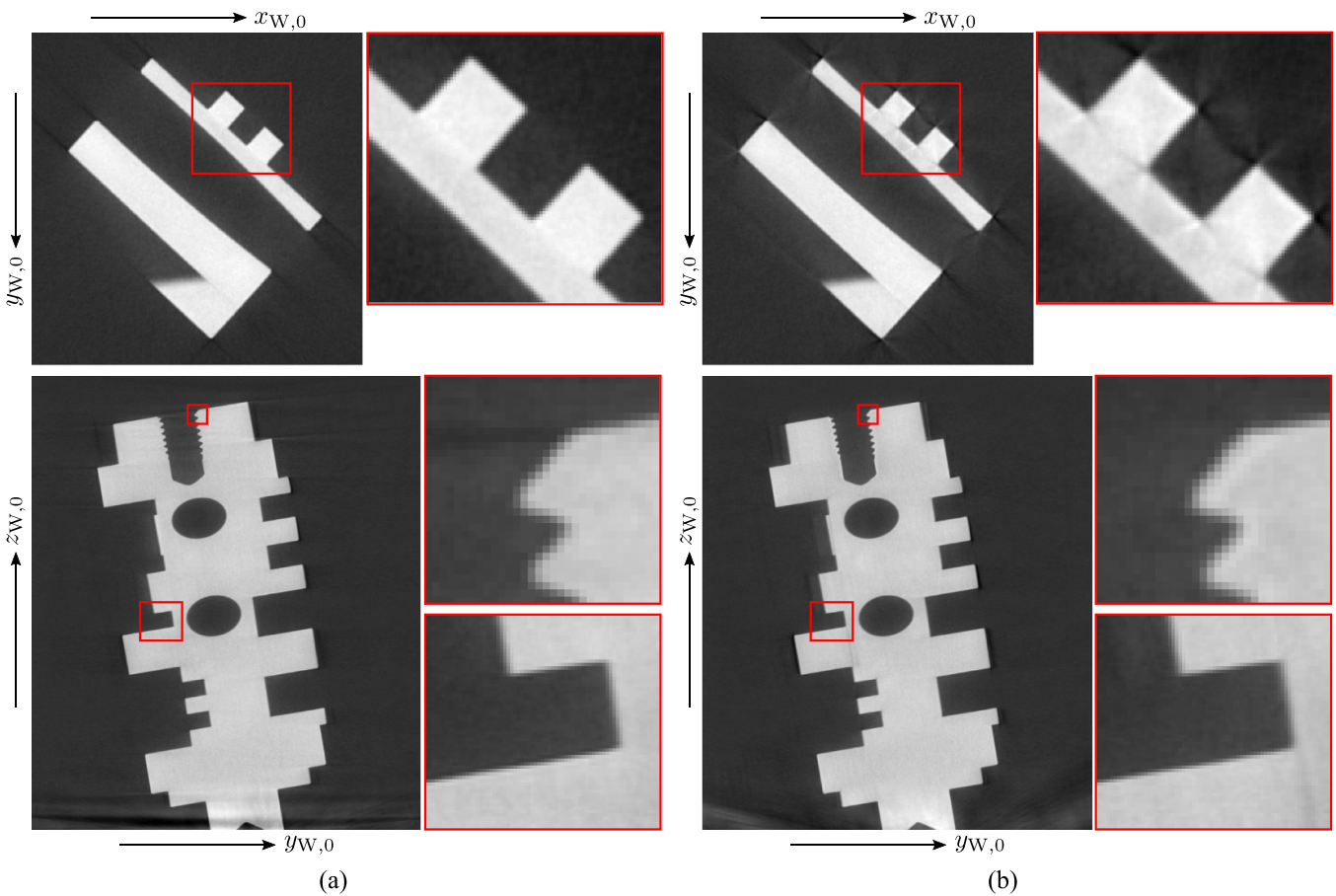


Figure 11. Slices through the reconstructed volume data of the multi-feature specimen. (a) Circular scan trajectory. (b) 3D scan trajectory. The gray values are linearly scaled between the minimum (black) and the maximum (white) intensity value of the full slice image, respectively.

measurement errors. Probing points for CT were homogeneously distributed on the full sphere surface with a safety distance of 0.5 mm from areas with a surface gradient above 15° . It should be mentioned that the CT settings as well as the evaluation software and measuring strategy (e.g. number and distribution of probing points) for the multi-sphere length standard differ from the presented configuration when the identical object is used for conformity assessment of CT devices. Results presented here can therefore not be directly used to rate the accuracy of the used device. Yet, it was tested that the choice of the evaluation software and the measurement strategy did not change the key findings.

6.3. Results and discussion

Figure 11 qualitatively compares the reconstructed volume data for the multi-feature specimen and the two different scan trajectories. The slices through the volume have an overall good quality for both the circular as well as the 3D scan trajectory. Though, the magnified views uncover streak-like imaging artifacts for the 3D scan trajectory (see magnified image section of the x - y -slice and lower section of the y - z slice). On the other hand, cone-beam artifacts in the area of the thread hole (see upper image section of the y - z slice) are only present

for the circular scan trajectory, as the 3D trajectory satisfies the sufficiency condition [22].

From the slice images, it is difficult to infer the influence of the scan trajectory on the accuracy of the surface determination. A more suitable assessment basis is given by the color coded surface errors from the target-actual comparison in figure 12. It is clearly visible that the result from the 3D scan trajectory shows overall higher errors, especially for the two cylindrical surface areas on the top and bottom of the part. In fact, the periodicity of the tilt angle variation equation (11) leads to periodically alternating positive and negative surface errors along the circumference. The maximum absolute surface error in these cylindrical areas is around $90\ \mu\text{m}$. In other areas, e.g. at the six cuboids in the left view in figures 12(a) and (b) respectively, the errors are in a comparable range in comparison to the circular scan, but still with slightly higher values (maximum absolute surface error of roughly $18\ \mu\text{m}$).

The results for the analyzed dimensional measurands figure 13 support the finding of higher errors for the 3D scan trajectory. In figure 13, the measurement errors are additionally differentiated between results that arise if the first single sphere calibration run (before the measurement scan) is used and results that arise using the second calibration run. It is visible that the differences between these two cases are

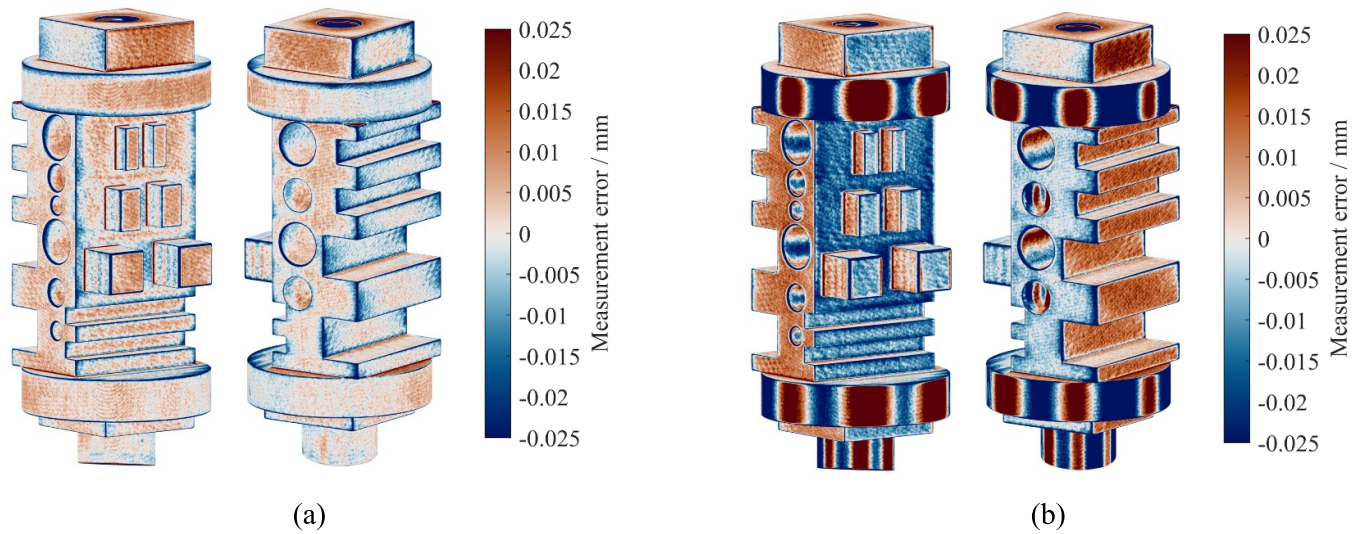


Figure 12. Target-actual comparison for the measured surface of the multi-feature specimen. (a) Circular scan trajectory. (b) 3D scan trajectory. For better comparability, the color map ('vik' from [23]) is cropped at $\pm 25 \mu\text{m}$ respectively.

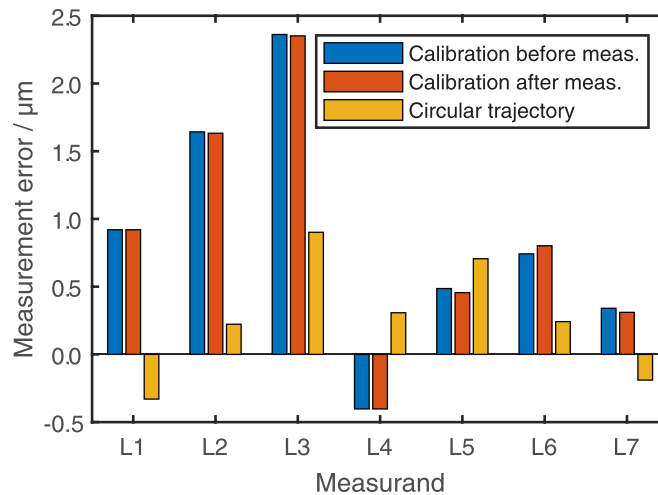


Figure 13. Measurement errors for the length features of the multi-feature specimen. The blue and red bars belong to reconstructions for the 3D scan trajectory based on different calibration runs.

negligible. This suggests that the repeatability of the hexapod positioning as well as the optimization is sufficient for the calibration procedure. While random positioning errors might not be significant for the influence of the calibration procedure on measurement errors, they could still affect the repeatability of the measurement scan in a significant manner. However, results from repeated measurements in our former work [8] (using the same hexapod and measurement object) suggest that this is not the case.

Overall, as already observed from the slice images in figure 11 and the target-actual comparison in figure 12, the quality of the reconstruction result and consequently the absolute dimensional measurement errors are inferior to the results from the circular trajectory. As already discussed in section 5.2, it is assumed that this is mainly caused by discrepancies between the calculated and true hexapod poses arising from an inaccurate (still reproducible) tilting around

the hexapod axes. Indeed, test measurements of the part with 3D scan trajectory using the multi-sphere calibration technique of [8] (not presented in this paper) did not show the periodic surface errors of figure 12 and also not that high errors for the measurands. As the multi-sphere calibration method compensates for systematic positioning errors, this supports the hypothesis.

Next, the dimensional measurement results for the multi-sphere length standard are presented. Figure 14 shows the measurement errors for the sphere distances. For a better assessment of the magnitude, the plots also contain the maximum permissible error (MPE) according to [24] that is stated by the supplier of the CT device. The results obtained with both scan trajectories are below the MPE and in a typical range compared to monitoring measurements that are regularly conducted with multi-sphere length standards of the same type. The overall absolute errors for the two different

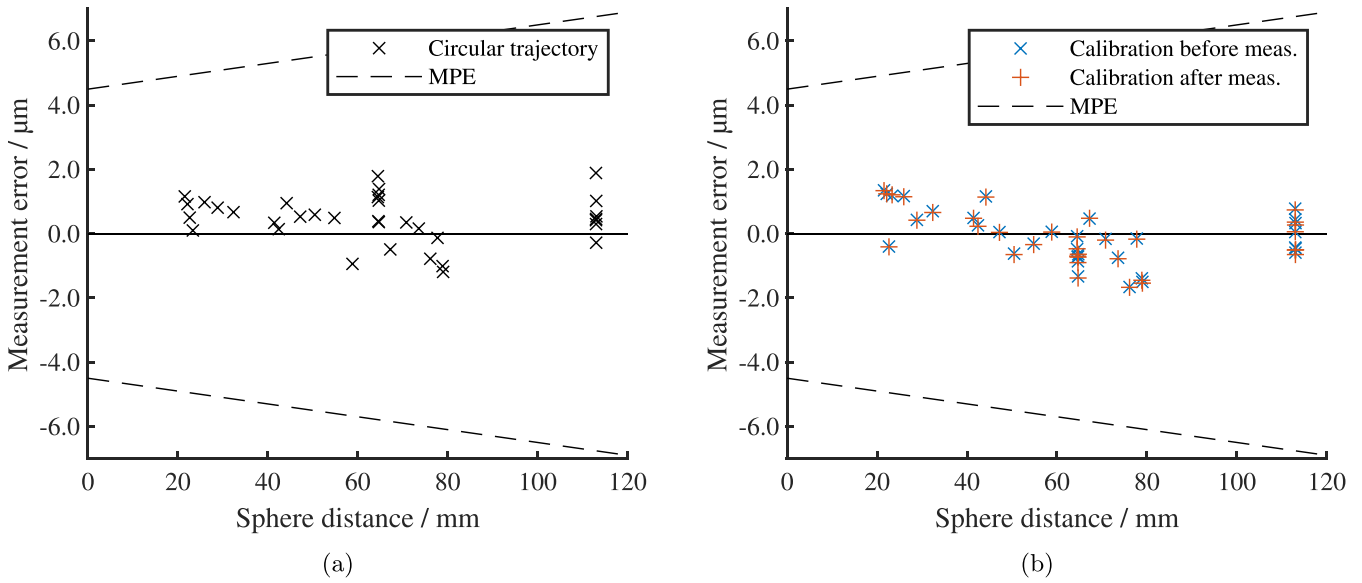


Figure 14. Measurement errors for the sphere distances of the multi-sphere length standard. (a) Circular scan trajectory. (b) 3D scan trajectory. For the 3D scan trajectory, the reconstruction was done twice, using the results from the single sphere calibration before and after the measurement scan.

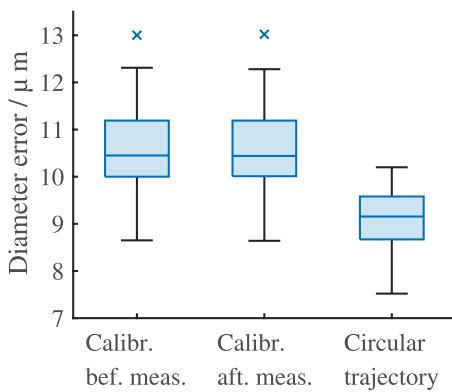


Figure 15. Measurement errors for the sphere diameters of the multi-sphere length standard.

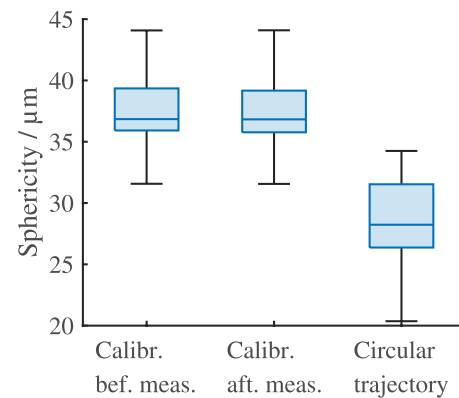


Figure 16. Sphericity values for the multi-sphere length standard.

trajectory types are in a comparable range. In agreement to the findings from the multi-feature specimen, the results for the 3D trajectory based on different calibration runs are nearly identical.

Sphere distance measurements allow for the judgment of scaling errors, but are more robust with regard to form errors. Therefore, also the sphere diameters figure 15 and the sphericity values figure 16 were measured.

The same characteristic result can be obtained from both figures: The circular scan trajectory leads to lower errors. This might be due to the already discussed absolute positioning errors, but also possibly from random errors due to the finite positioning repeatability or thermal influences of the hexapod motors. Again, the chosen calibration run (before or after the measurement scan) has no effect on the results. It should be mentioned that cone-beam artifacts, which generally arise for circular CT measurements of balls, do only have a minor effect for the investigated object and geometry setting. Accordingly,

a reduction of form errors, which could potentially be reached with a 3D scan trajectory [8] by avoiding cone-beam artifacts, was not observed.

7. Summary

In this paper, we have presented a method to calibrate 3D scan trajectories for dimensional CT with a hexapod as 6-DOF object manipulator. The method is based on imaging a single metal ball and therefore represents a easy-to-implement alternative in comparison to methods based on multi-sphere objects that require calibration data. Keeping the intrinsic parameters of the CT device fixed, a one-step optimization approach was used to extract the geometry parameters of the hexapod coordinate system, which are required to compute the projection matrices for any scan trajectory. The projection matrices are necessary to correctly reconstruct the measurement volume.

The convergence of the optimization results towards the true geometry parameters was validated by means of simulation studies. The theoretically achievable accuracy was found to be limited by the detection accuracy for the projected ball midpoint in the x-ray images. The experimental validation yielded higher reprojection errors than the simulation studies, which was attributed to inaccuracies for rotations performed by the manipulator device. This was also assumed to be the major cause for comparatively high measurement errors when the method is applied to CT scans for dimensional measurements. Nevertheless, the overall accuracy might be sufficient for certain measurement tasks and is expected to increase for a higher pose accuracy of the manipulator system.

The presented calibration method could potentially be improved in terms of accuracy by mathematically correcting for absolute positioning errors. Further improvements could be obtained by additionally making use of the rotary table of the CT device or by using more than one sphere, but this would contradict the advantage of an easy implementation. Possible industrial fields of application for the version presented could therefore also be in the area of qualitative non-destructive testing with lower accuracy requirements.

The methodology can also be transferred to other object manipulator systems such as robotic arms and also to systems in which the x-ray source and the detector are moved and not the object. For systems with fixed source-detector-distance, as it is for example the case with C-arm CT devices, the method can be applied without major adaptations. The achievable accuracy for robot based setups however again depends on the positioning accuracy of the manipulator devices. While the pose repeatability of robot arms might be sufficient [2], comparatively high systematic deviations might make it more feasible to use calibration methods such as the multi-sphere based procedure in [8] that compensate for systematic errors.

Data availability statement

The data that support the findings of this study are available upon reasonable request from the authors.

Acknowledgments

Author contributions according to CRediT taxonomy [25] are as follows: L B contributed Conceptualization, Data curation, Formal Analysis, Investigation, Methodology, Project Administration, Software, Visualization, Writing—original draft as well as Writing—review & editing. A M M contributed Methodology, Software and Formal Analysis (Generation of the reference model for figure 12), Validation and Writing—original draft. T H contributed Funding acquisition, Resources, Supervision and Writing—review & editing.

The authors thank T Kistner (Kistner Metrologie Service GmbH) for the provision of additional reference measurements. The reconstruction software was kindly provided by Siemens Healthcare GmbH. P Kaller is thanked for his support with reference measurements. The authors would like to thank the German Research Foundation (DFG) for supporting the

research project ‘FOR 2271: process-oriented tolerance management based on virtual computer-aided engineering tools’ under Grant Number HA 5915/9-2 and the research project TRR 285—project-ID 418701707—subproject C05. The acquisition of the CT system Metrotom 1500 was financially supported by the DFG through Grant No. 324672600.

Appendix. Rotation matrices

A rotation matrix representing an orientation can be composed by three successive extrinsic rotations using the basic rotation matrices $\mathbf{R}_x(\alpha)$, $\mathbf{R}_y(\beta)$ and $\mathbf{R}_z(\gamma)$, which are defined as

$$\mathbf{R}_x(\alpha) = \begin{bmatrix} 1 & 0 & 0 \\ 0 & \cos \alpha & -\sin \alpha \\ 0 & \sin \alpha & \cos \alpha \end{bmatrix},$$

$$\mathbf{R}_y(\beta) = \begin{bmatrix} \cos \beta & 0 & \sin \beta \\ 0 & 1 & 0 \\ -\sin \beta & 0 & \cos \beta \end{bmatrix},$$

$$\mathbf{R}_z(\gamma) = \begin{bmatrix} \cos \gamma & -\sin \gamma & 0 \\ \sin \gamma & \cos \gamma & 0 \\ 0 & 0 & 1 \end{bmatrix}.$$

Different rotation sequences based on these basic rotations can be chosen. Especially if rotation angles have to be found by optimization, the choice should be made in a way that ambiguities due to gimbal lock (second rotation angle at $\pm 90^\circ$) are avoided. In our case, we used rotation sequences $\mathbf{R} = \mathbf{R}_x(\alpha)\mathbf{R}_y(\beta)\mathbf{R}_z(\gamma)$, which are also used by the hexapod controller. Using the abbreviations s for the sine function and c for the cosine function, the matrix \mathbf{R} is given by

$$\begin{aligned} \mathbf{R} &= \mathbf{R}_x(\alpha)\mathbf{R}_y(\beta)\mathbf{R}_z(\gamma) \\ &= \begin{bmatrix} c\beta c\gamma & -c\beta s\gamma & s\beta \\ c\alpha s\gamma + s\alpha s\beta c\gamma & c\alpha c\gamma - s\alpha s\beta s\gamma & -s\alpha c\beta \\ s\alpha s\gamma - c\alpha s\beta c\gamma & c\alpha s\beta s\gamma + s\alpha c\gamma & c\alpha c\beta \end{bmatrix}. \end{aligned}$$

Note that rotation sequences are also sometimes given as intrinsic (local) rotations, i.e. rotating around the moved axes. This results in an inverted order of basic rotations.

From an existing rotation matrix \mathbf{R} , the rotation angles from $\mathbf{R} = \mathbf{R}_x(\alpha)\mathbf{R}_y(\beta)\mathbf{R}_z(\gamma)$ can be extracted from single entries of the matrix (see e.g. [26]). From $R^{1,3} = \sin \beta$, there are two possible solutions for β between $-\pi$ and π . If we restrict the range to $-\pi/2 \leq \beta \leq \pi/2$, the solution can be calculated by

$$\beta = \arcsin R^{1,3}.$$

Provided that $\beta \neq \pm\pi/2$ (no gimbal lock), the angles α and γ are determined by

$$\begin{aligned} \cos \gamma &= \frac{R^{1,1}}{\cos \beta}, & \sin \gamma &= -\frac{R^{1,2}}{\cos \beta}, \\ \cos \alpha &= \frac{R^{3,3}}{\cos \beta}, & \sin \alpha &= -\frac{R^{2,3}}{\cos \beta}. \end{aligned}$$

These equations can be solved using the atan2 function [27]:

$$\gamma = \operatorname{atan2}\left(-\frac{R^{1,2}}{\cos\beta}, \frac{R^{1,1}}{\cos\beta}\right),$$

$$\alpha = \operatorname{atan2}\left(-\frac{R^{2,3}}{\cos\beta}, \frac{R^{3,3}}{\cos\beta}\right).$$

ORCID iDs

Lorenz Butzhammer  <https://orcid.org/0000-0002-5537-4849>

Andreas Michael Müller  <https://orcid.org/0000-0002-3213-309X>

Tino Hausotte  <https://orcid.org/0000-0002-2923-3217>

References

- [1] Ametova E, Probst G and Dewulf W 2018 X-ray computed tomography devices and their components *Industrial X-Ray Computed Tomography* ed S Carmignato, W Dewulf and R Leach (Cham: Springer) pp 69–98
- [2] Hiller J, Landstorfer P, Marx P and Herbst M 2020 Evaluation of the impact of faulty scanning trajectories in robot-based x-ray computed tomography *Meas. Sci. Technol.* **32** 015401
- [3] Kang R, Probst G M, Slaets P and Dewulf W 2020 Investigation of the impact of various robot properties on a twin Robot-CT system *Nondestruct. Test. Eval.* **35** 276–86
- [4] Ziertmann A, Jahnke P, Kerscher S, Koch M and Holub W 2020 Robot guided computed tomography *J. Japan Soc. Precis. Eng.* **86** 316–22
- [5] Fischer A, Lasser T, Schrapp M, Stephan J and Noël P B 2016 Object specific trajectory optimization for industrial x-ray computed tomography *Sci. Rep.* **6** 19135
- [6] Bauer F, Goldammer M and Grosse C U 2021 Selection and evaluation of spherical acquisition trajectories for industrial computed tomography *Proc. R. Soc. A* **477** 20210192
- [7] Herl G, Hiller J, Thies M, Zaech J N, Unberath M and Maier A 2021 Task-specific trajectory optimisation for twin-robotic x-ray tomography *IEEE Trans. Comput. Imaging* **7** 894–907
- [8] Butzhammer L and Hausotte T 2021 Complex 3D scan trajectories for industrial cone-beam computed tomography using a hexapod *Meas. Sci. Technol.* **32** 105402
- [9] Li X, Zhang D and Liu B 2010 A generic geometric calibration method for tomographic imaging systems with flat-panel detectors—a detailed implementation guide *Med. Phys.* **37** 3844–54
- [10] Hartley R and Zisserman A 2003 *Multiple View Geometry in Computer Vision* 2nd edn (Cambridge, MA: Cambridge University Press)
- [11] Bircher B A, Meli F, Küng A and Thalmann R 2019 CT geometry determination using individual radiographs of calibrated multi-sphere standards *9th Conf. on Industrial Computed Tomography (iCT 2019) (Padova, Italy)*
- [12] Ferrucci M, Dewulf W and Dönmez A 2021 Measurement of sample stage error motions in cone-beam x-ray computed tomography instruments by minimization of reprojection errors *Precis. Eng.* **67** 48–57
- [13] Kang R, Probst G, Vlaeyen M, Fei G, Guerrero P, Haitjema H, Slaets P and Dewulf W 2022 Geometric qualification for robot CT with flexible trajectories *11th Conf. on Industrial Computed Tomography (iCT 2022) (Wels, Austria)*
- [14] Blumensath T, O'Brien N and Wood C E 2018 Calibration of robotic manipulator systems for cone-beam tomography imaging *IEEE Trans. Nucl. Sci.* **65** 1384–93
- [15] Wood C E, O'Brien N, Denysov A and Blumensath T 2019 Computed laminography of CFRP using an x-ray cone-beam and robotic sample manipulator systems *IEEE Trans. Nucl. Sci.* **66** 655–63
- [16] Deyhle H, Towsyfyan H, Biguri A, Mavrogordato M, Boardman R and Blumensath T 2020 Spatial resolution of a laboratory based x-ray cone-beam laminography scanning system for various trajectories *NDT&E Int.* **111** 102222
- [17] Metzner S and Hausotte T 2019 Automatic camera calibration and sensor registration of a multi-sensor fringe measurement system using hexapod positioning *Proc. SPIE* **11056** 1105616
- [18] DIN 5401:2002-08 2002 *Rolling Bearings—Balls for Rolling Bearings and General Industrial Use* (Deutsches Institut für Normung)
- [19] Deng L, Xi X, Li L, Han Y and Yan B 2015 A method to determine the detector locations of the cone-beam projection of the balls' centers *Phys. Med. Biol.* **60** 9295–311
- [20] Butzhammer L, Müller A M and Hausotte T 2020 Comparison of geometrically derived quality criteria regarding optimal workpiece orientation for computed tomography measurements *10th Conf. on Industrial Computed Tomography (iCT 2020) (Wels, Austria)*
- [21] Müller A M and Hausotte T 2022 Improving template-based CT data evaluation by integrating CMM reference data into a CAD model-based high fidelity triangle mesh *Nondestruct. Test. Eval.* **37** 692–706
- [22] Tuy H 1983 An inversion formula for cone-beam reconstruction *SIAM J. Appl. Math.* **43** 546–52
- [23] Cramer F 2018 Scientific colour maps (available at: <http://doi.org/10.5281/zenodo.1243862>) (Accessed 8 June 2022)
- [24] VDI/VDE 2630 Part 13 2011 Computed tomography in dimensional measurement—guideline for the application of DIN EN ISO 10360 for coordinate measuring machines with CT sensors
- [25] CASRAI CRediT (available at: www.casrai.org/credit.html) (Accessed 5 September 2022)
- [26] Woernle C 2011 *Mehrkörpersysteme* (Berlin: Springer)
- [27] The MathWorks, Inc atan2 four-quadrant inverse tangent (available at: <https://de.mathworks.com/help/matlab/ref/atan2.html>) (Accessed 5 September 2022)